Nanoscale

Accepted Manuscript

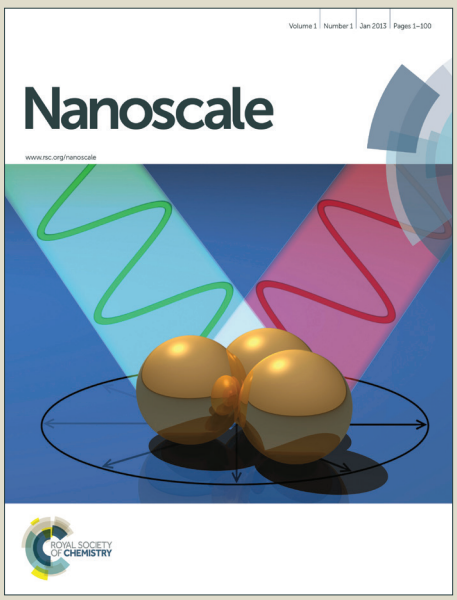

ROYAL SOCIETY OF CHEMISTRY

www.rsc.org/nanoscale

Journal Name

RSCPublishing

ARTICLE

Tungsten trioxide nanoplate array supported platinum as highly efficient counter electrode for dye-sensitized solar cells

Cite this: DOI: 10.1039/x0xx00000x

Received 00th January 2012,
Accepted 00th January 2012

DOI: 10.1039/x0xx00000x

www.rsc.org/

Dandan Song,[a] Peng Cui,[a] Xing Zhao,[a] Meicheng Li,[a, b*] Lihua Chu,[a] Tianyue Wang[a] and Bing Jiang[a]

Tungsten trioxide (WO_3) nanoplate array is fabricated directly on FTO/glass substrate and used as platinum (Pt) nanoscale supporter for highly efficient and low Pt-consumption counter electrode (CE) of dye-sensitized solar cells (DSCs). Pt/WO_3 composite structure, with Pt nanoparticles in diameter of 2-3 nm, increases the electrochemical catalytic activity in catalyzing the reduction of triiodide. Accordingly, the power conversion efficiency is increased from less than 1% for WO_3 CE and 8.1% for Pt CE, respectively, to 8.9% for Pt/WO_3 CE. Moreover, the use of Pt/WO_3 CE can dramatically reduce the consumption of scarce Pt material, with a quite low Pt-loading of ~ 2 μg/cm^2, while keep a much better performance. The excellent performance of Pt/WO_3 CE is attributed to the efficient electron injection and transport via WO_3 supporters, as well as the nanostructure array morphology of WO_3 for deposition of fine Pt nanoparticles. This work provides an approach for developing highly catalytic and low-cost Pt based CEs, which also has implications for the development of Pt/WO_3 nanoplate array for other applications.

1. Introduction

Dye-sensitized solar cells (DSCs) have been rapidly developed in recent years for their unique advantages including low-cost, high energy conversion efficiency and simple production procedure.[1-3] Counter electrode (CE), catalyzing the reduction of triiodide, is one of the important components in the DSC. Despite of the increasing studies in alternative CEs, such as carbonaceous nanomaterials,[4] transition metal sulfides/nitrides,[5] polymers, and their composites,[6,7] the most commonly used and efficient CE is still platinum (Pt) CE which exhibits high catalytic activity for triiodide reduction. As Pt is scarce and expensive, the reducing in the usage of Pt in CE is crucial for lowering the cost of DSCs. Increasing the catalytic activity of Pt CE while keeping low Pt-loading is of great importance for highly efficient and low-cost DSCs.

The catalytic activity of Pt CE is determined by the catalytic surface area confined by the total surface area of Pt nanoparticles. Recent studies also demonstrate that the catalytic activity of Pt CE and the power conversion efficiency (PCE) of the corresponding DSC can be improved by optimizing the morphology of Pt.[8-10] However, Pt nanoparticles tend to agglomerate due to the fast diffusion and coalescence of metal atoms on the substrate surface even when the thickness of Pt film is thin.[11,12] The dispersion of Pt inside the nanoscale supporters will reduce its agglomeration and thus increase the effective electrocatalytic area due to the large specific surface area of supporters, which thereby will lead to high catalytic activity. Therefore, a few of attempt were carried out using carbonous nanomaterials or some metal compounds (e.g. TiO_2) as nanoscale supporters.[13-15] Nevertheless, the supporters fabricated from powder (such as graphene) face challenges in adhesion with the underneath fluorine doped tin oxide (FTO)/glass substrates and thus in the long term stability. Ordered nanostructures directly growing on FTO substrates will debarb this problem whereas keep the advantages of nanoscale supporters, and offer the distinct advantage of ready integration into a device architecture for electronic, electrochemical catalytic and optical applications. Thus, they are potential to be more suitable for constructing composite CEs with Pt for highly efficient DSCs.

Moreover, to reduce Pt-loading, the nominal thickness of Pt needs to be as thin as possible. Studies show that nominal Pt thickness of 1-3 nm is more efficient than thicker Pt films.[16] With such low Pt-loading, Pt nanoparticles are inconsecutive, and in Pt/supporter CE, the electrons need to be injected and transported via the supporter from FTO to inconsecutive Pt nanoparticles. Therefore, the electronic properties of the supporter, though rarely been concerned, will also play

important roles in determining the catalytic performance of composite CEs.

Tungsten trioxide (WO_3) is a versatile material, and has attracted considerable attention due to its applications in electrochromic, photocatalytic, and gas sensing materials.[17,18] In addition, WO_3 is n-type semiconductor with inherently good electron transport property, and its conduction band can provide enough potential for electron injection from FTO and to Pt since it is located at approximately 0.3 eV versus NHE.[19,20] Hence, WO_3 is probably able to mediate electron injection and transport from FTO to Pt. However, unlike TiO_2, the direct growth of WO_3 nanostructure array on FTO/glass using facile hydrothermal method is hard to be achieved due to the uneven deposition of WO_3 on FTO/glass.[20-22] The fabrication procedures generally employ a WO_3 seed layer which introduces grain boundaries.[21] Thereby, it is considered to be important to control the growth of vertically nanostructured WO_3 arrays directly on FTO/glass substrates to accelerate electron transport between FTO and WO_3.

Hence, in this work, a procedure for the direct growth of WO_3 nanostructure array was proposed using hydrothermal method. Then the as-prepared WO_3 nanoplate array is opted to incorporate with Pt as highly efficient CE for DSCs. As expected, DSC using WO_3 nanoplate array supported Pt as CE shows obviously higher efficiency than that using pristine Pt CE. The factors for the improvements have been investigated.

2. Experimental

1. Synthesis of WO_3 on FTO glass

In a typical synthesis, 0.231 g of sodium tungstate ($Na_2WO_4{\cdot}2H_2O$) was dissolved in 15 ml de-ionized water. 5 ml HCl (3mol/L) aqueous solution was added to the above solution and stirred, and then yellow precipitate gradually formed in the solution. Different amount of oxalic acid ($H_2C_2O_4$) was added to above solution to control the thickness of the WO_3 film on FTO. Then 1.260 g of ammonium sulfate ($(NH4)_2SO_4$) was added to the mixed solution followed by stirring for 30 min. After stirring, the mixed solution was diluted to 40 ml with de-ionized water and subsequently transferred to a 50ml Teflon-lined autoclave. FTO/glass substrates, which were previously cleaned and treated with ozone, were placed in the autoclave with FTO side facing down. The hydrothermal synthesis was carried out at 180 °C for 8 h. After cooled down to room temperature, FTO/glass substrates covered by WO_3 film were taken out and rinsed with de-ionized water, followed by dried at 60 °C for 12h.

2. Fabrication of counter electrode and DSCs

Pt and Pt/WO_3 CEs were fabricated by sputtering Pt on pristine and WO_3 coated FTO/glass substrates, respectively. The sputtering was conducted using a DC sputtering system (Quorum Q150TS) in the conditions of a sputtering current of 10 mA, a working gas (Ar, 99.999%) pressure of 0.01 mbar, a target to substrate working distance of 54 mm and a period of 20-60 seconds without substrate heating (corresponding to nominal thickness of 1-3 nm and a Pt-loading of 2-6 μg/cm^2). TiO_2 mesoporous layer and scattering layer were prepared by doctor-blading of TiO_2 nanoparticle (P25) slurry and TiO_2 microsphere (200 nm in diameter) slurry subsequently on FTO/glass substrates, respectively. All of the TiO_2 films were post-treated with $TiCl_4$. After calcination, TiO_2 films were immersed in 0.3 mmol/l ethanol solution of N719 dye for 24 hours. DSCs were fabricated by assembling dye-sensitized TiO_2 photoanodes with as-fabricated CEs using 30 μm thick Surlyn. I^-/I_3^- electrolyte with acetonitrile as the solvent was used. Symmetric cells for electrochemical measurements were fabricated by assembling two identical CEs together using 30 μm thick Surlyn.

3. Characterization

The structure and morphology of the materials were characterized by X-Ray Diffraction (XRD, Shimadzu XRD-6000), transmission electron microscopy (TEM, FEI Tecnai F20), scanning electron microscopy (SEM, FEI Quanta 200F), and atomic force microscope (AFM, Agilent 5500). Current density-voltage curves of DSCs were measured using a source meter (Keithley 2400) under AM 1.5G irradiation with a power density of 100 mW/cm^2 from a solar simulator (XES-301S+EL-100). Electrochemical impedance spectroscopy was carried out using the electrochemical workstation (CHI660D), performed on symmetric cells. The frequency range varied from 100 kHz to 0.1 Hz.

3. Results and discussion

FTO/glass substrates were primarily treated by ozone to form uniform hydrophilic surface for the homogeneous nucleation of WO_3 molecules from the aqueous solution in the initial step. The formation of WO_3 from a tungstate ion solution using concentrated acid can be explained from the following equations:[23]

$$Na_2WO_4+2H^+ \rightarrow H_2WO_4+2Na^+$$

$$H_2WO_4 \rightarrow WO_3 + H_2O$$

It is observed that the yellow precipitate of H_2WO_4 generated from 0.231 g $Na_2WO_4{\cdot}2H_2O$ is not able to be solved totally without the presence of oxalic acid ($H_2C_2O_4$). Hence, different amount of $H_2C_2O_4$ (0-0.630 g) was added to the reaction solution to control the concentration of H_2WO_4 and the generation rate of WO_3. SEM images of as-prepared WO_3 on FTO are shown in Fig.1. It is clear that the presence of $H_2C_2O_4$ in reaction solution is critical in the growth of WO_3 nanostructure array. With increasing the concentration of $H_2C_2O_4$, different nanostructures, including nanobelts, novel hierarchical flower-like structure constructed by nanobelts and nanowires, and plate-like nanostructures, can be obtained on FTO/glass substrates. It is found that these WO_3 films perform good adhesion with FTO/glass substrate as evidenced by conventional tape tests, which benefits for the long-term stability of the related DSCs. These WO_3/FTO/glass samples with different WO_3 morphologies are supposed to possess different properties. In the present case, WO_3 nanostructure

array is used as Pt supporters and electron transport material, the plate-like WO_3 nanostructure array (Shown in Fig. 1d and 1i, defined as WO_3 nanoplate array) with direct transport path, facilitated by its plate-like structure and vertical growth on FTO, is more suitable and is opted to incorporated with Pt as counter electrodes (CEs).

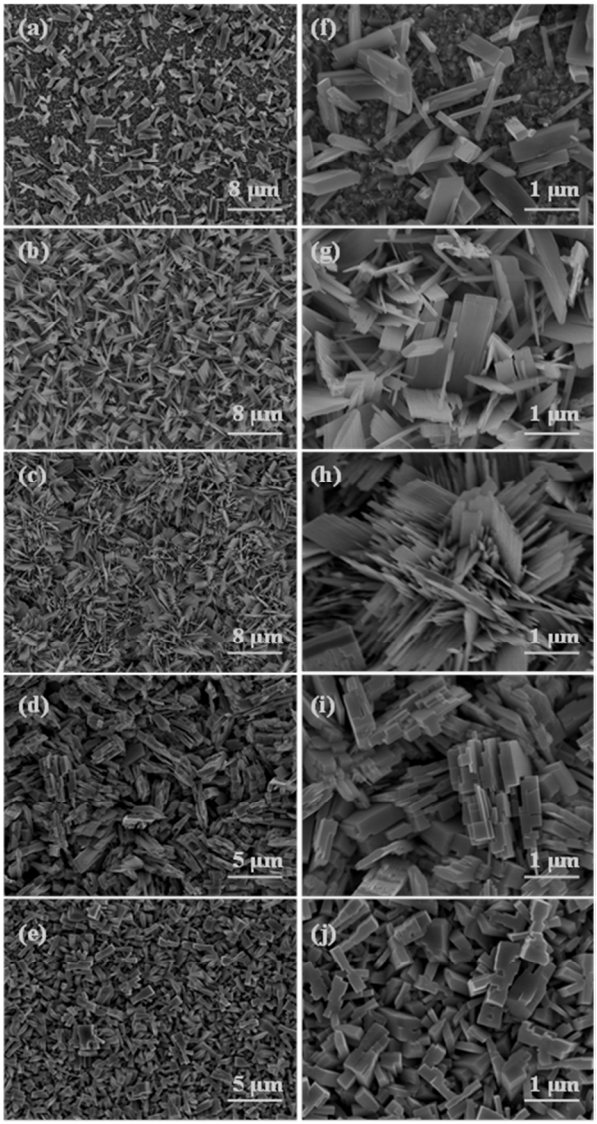

Fig. 1 SEM images of WO_3 on FTO/glass substrates fabricated at different concentration of $H_2C_2O_4$, (a) 0 g, (b) 0.140 g, (c) 0.210 g(d) 0.315 g and (e) 0.630g. (f-j) are the corresponding high magnification images of (a-e)

To achieve a high surface area, a porous layer of WO_3 nanoplate array was prepared by decreasing the concentration of the reactants. SEM image of as-prepared WO_3 is shown in Fig. 2a. WO_3 still exhibits plate-like structure with nanoscale structures on its surface, and WO_3 array grows vertically to the FTO/glass substrate. The XRD patterns of the as-prepared WO_3 product show that it is consisted of WO_3 and $WO_3 \cdot 0.33H_2O$ (Fig. S1 in the Supplementary Information). WO_3 exhibits a monoclinic structure (JCPDS no. 431035) while $WO_3 \cdot 0.33H_2O$ is an orthorhombic-type structure (JCPDS no. 350270). TEM image of the WO_3 nanoplate shown in Fig. 2b indicates that the WO_3 nanoplate is composed of multi-layers of WO_3 sheets which provide large surface area for Pt deposition.

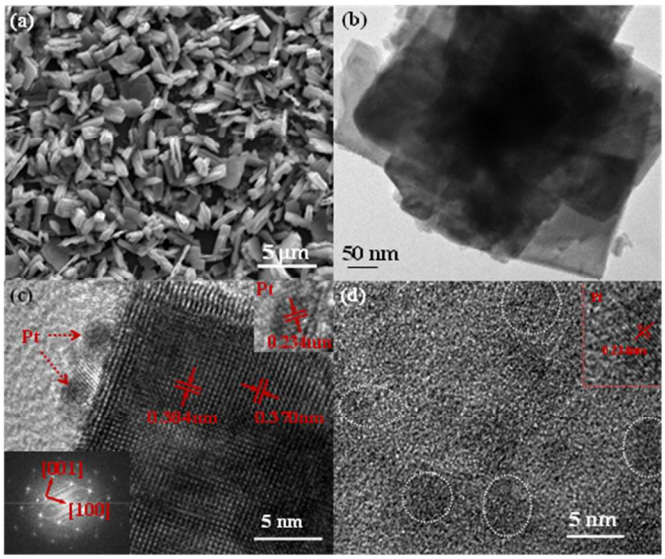

Fig. 2. (a) SEM image of WO_3 nanoplate array with a thickness of ~600 nm; (b) TEM of the typical WO_3 nanoplate; (c) HRTEM (HRTEM) of Pt (1nm)/WO_3, insets are the SAED pattern of WO_3 and the magnification image of a Pt nanoparticle; (d) HRTEM of Pt (1nm)/FTO, inset is the magnification image of a Pt nanoparticle.

After sputtering a spot of Pt, the surface of WO_3 is decorated by Pt nanoparticles. To achieve a low Pt consumption, the sputtering period of Pt is controlled to be 20 s (corresponding to a nominal thickness of 1 nm and a low Pt-loading of ~ 2 μg/cm^2). SEM image of Pt/WO_3 electrode was also characterized, which exhibited a similar morphology to the pristine WO_3 electrode and was not shown here. Fig. 2c shows the high resolution transmission electron microscopy (HRTEM) image of Pt/WO_3. The lattice spacing of WO_3 nanoplate is around 0.384 and 0.370 nm, which are extremely close to the values of (002) and (200) lattice spacing, respectively, according to JCPDS card no. 431035. The lattice spacing of Pt nanoparticles is around 0.234 nm, which corresponds to its (111) lattice spacing. It also displays that Pt nanoparticles, 2-3 nm in diameter, distribute discretely on WO_3 surface. Therefore, they are hard to be identified in SEM images. The Pt nanoparticles directly deposited on FTO/glass substrates have also been characterized by HRTEM and shown in Fig. 2d. It can be seen that the morphology of the Pt nanoparticles are not regular and the size is also larger than that on WO_3 nanoplate, which probably due to the coalescing of the Pt nanoparticles on FTO surface. This observation is similar to a previous report in which revealed that Pt particles begin coalescing when the nominal thickness of Pt was thicker than 0.75 nm using TEM technique.[11] For further evaluating the impact of WO_3 supporter on the morphology of Pt, a larger amount of Pt (3 nm) was also

deposited on FTO and WO_3 nanoplate supporter. HRTEM images (Fig. S2) clearly reveal the coalescing of Pt nanoparticles on FTO surface, whereas on WO_3 surface, the Pt nanoparticles are distributed discretely with diameters in the range of 2-5 nm. In addition, AFM and kelvin potential force microscope (KPFM) (Fig. S3) were also employed, which also indicate that Pt nanoparticles distribute heterogeneously on FTO surface even in the case of Pt film with 1 nm nominal thickness.

The small size of Pt nanoparticles in Pt/WO_3 CE is probably due to the increased deposition area for Pt on WO_3 surface, which avoids the aggregation of Pt nanoparticles and benefit for deposition of fine Pt nanoparticles. In a DSC, the oxidized site (I_3^-) of the redox couple captures two electrons from CE and is reduced to $3I^-$. As the catalytic surface is confined by the total surface area of Pt nanoparticles, the catalytic surface in Pt/WO_3 CE will be increased due to the formation of fine Pt nanoparticles. Meanwhile, the porous WO_3 film benefits the diffusion of I^-/I_3^- redox couple. Therefore, the use of Pt/WO_3 CE will be potential to improve the photovoltaic performance of the related DSC.

The photocurrent density-voltage curves (J-V) of the DSCs using different CEs are shown in Fig. 3. The photovoltaic parameters including the short circuit current density (J_{SC}), the open circuit voltage (V_{OC}), the fill factor (FF) and the power conversion efficiency (PCE) are extracted from the J-V curves and summarized with the standard deviations (J-V curves with error bars are shown in Fig. S4) in Table 1. As expected, the J_{SC} is obviously higher for DSC using Pt/WO_3 CE (17.9 mA/cm^2) than that using Pt CE (15.9 mA/cm^2) with the same consumption of Pt (with a nominal thickness of 1 nm). The FF and V_{OC} are similar in these two kinds of DSCs, as shown in Table 1. As a result, the PCE is increased from 8.1% for Pt CE to 8.9% for Pt/WO_3 CE. The calculated standard deviation of the PCE from these two kinds of DSCs are around 0.1%, indicating that the significant difference (0.8%) in PCE of DSCs with or without WO_3 supporter is due to the intrinsic kinetics other than experimental errors. It is demonstrated that Pt (1nm)/WO_3 CE is also more efficient than the best performed Pt/FTO CE with an optimized Pt thickness (as shown in Fig. S5a). When the nominal thickness of Pt is increased to an optimized value of 3 nm (sputtered for 60 s), J_{SC} and PCE are only slightly higher over these of DSC using 1 nm thick Pt CE. Pt/WO_3 CE is the most efficient, despite of the much lower Pt-loading in Pt/WO_3 CE (sputtered for 20 s). The improvements in cell performance agree with the formation of the fine and discrete Pt nanoparticles on WO_3 nanoplate surface. Therefore, the use of WO_3 nanoplate array as Pt support is efficient in enhancing the photovoltaic performance of DSC and reducing the consumption of scarce Pt material, demonstrating the high potential of Pt/WO_3 CE for the use in highly efficient and low-cost DSCs.

In addition, it is also proved that WO_3 array is critical for the efficiency improvement. WO_3 nanoparticles have also been used as Pt supporters, but the related DSCs present no improvements in photovoltaic performance even with a quite thin WO_3 nanoparticle film (<400 nm) (Fig. S5b). The efficacy difference of WO_3 nanoplate array and nanoparticle film in improving the performance of DSCs is related to their different electrical properties and will be discussed in the later part. Besides, it is found that the DSC using pristine WO_3 generally yields a low FF less than 10% and a PCE less than 1% (Fig. S5b), indicating the poor catalytic activity of WO_3 for triiodide reduction. Moreover, the impact of the WO_3 on the stability of the DSCs has also been investigated at elevated temperature (as shown in Fig. S6). It is observed that the loss of the PCE due to the high temperature ageing is similar in DSCs using Pt CE and Pt/WO_3 CE, implying that the introduce of WO_3 in the CE has not caused additional degradation processes.

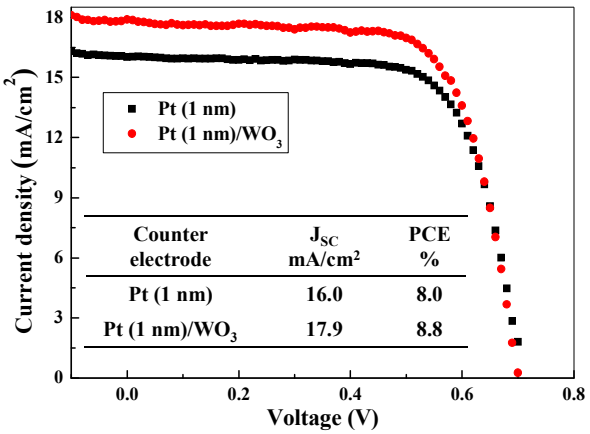

Fig. 3. J-V curves of DSCs using Pt and Pt/WO_3 nanoplate array CEs, respectively.

Table 1 Photovoltaic parameters of DSCs using different CEs and EIS parameters of symmetric cells with two identical CEs[a]

CE	J_{SC}	V_{OC}	FF	PCE	R_S	R_{ct2}	J_0
Pt	15.9	0.72	71.1	8.1	5.22	0.90	6.7
	±0.2	*±0.01*	*±0.5*	*±0.1*	*±0.06*	*±0.02*	*±0.1*
Pt/WO_3	17.9	0.71	69.7	8.9	4.53	0.77	9.5
	±0.2	*±0.01*	*±0.5*	*±0.1*	*±0.17*	*±0.01*	*±0.5*

[a]The units of J_{SC}, V_{OC}, FF, PCE, R_S, R_{ct2} and J_0 are mA/cm^2, V, %, %, $\Omega \cdot cm^2$, $\Omega \cdot cm^2$ and mA/cm^2, respectively. The standard deviations of the parameters were calculated from two or more identical cells.

It is obvious that the higher J_{SC} using WO_3/Pt CE is responsible for the higher efficiency. As the DSCs have universal photoanodes but different CEs, the photo-generated current (I_{ph}) from these DSCs shall have less difference. Hence, the difference in J_{SC} is mainly caused by the series resistance of the device, and a larger J_{SC} corresponds to a lowered series resistance. In a DSC, with the equivalent circuit depicted in Fig. 4a, the series resistance is composed of the series resistance at the FTO/electrode contact and in the electrode (R_S), the charge

transfer resistance at electrolyte/CE interface (R_{ct2}), and the Nernst diffusion impedance of redox couple in the electrolyte (Z_N).[24]

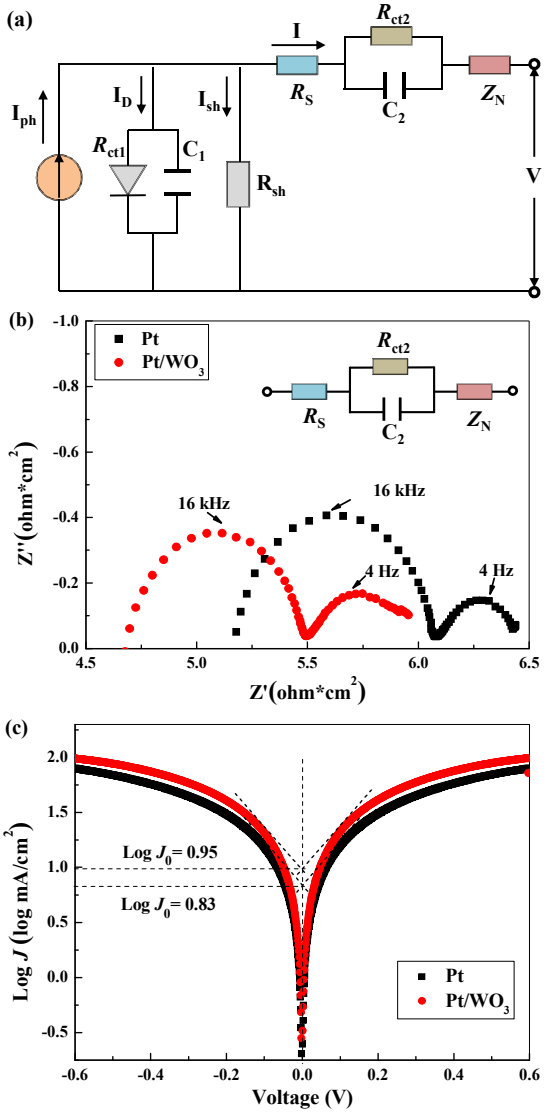

Fig. 4. (a) Equivalent circuit of a DSC; (b) Nyquist plots and (c) Tafel polarization curves of the symmetric cells with two identical CEs of Pt (1nm) and Pt (1nm)/WO_3, respectively.

To study the kinetics in determining the differences of the series resistance between the DSCs, symmetric cells, with the equivalent circuit (shown in Fig. 4b inset) containing all the elements in series resistance,[25,26] were fabricated with two identical CEs. Electrochemical impedance spectroscopy (EIS) was carried out and the Nyquist plots from different CEs are shown in Fig. 4b. The values of R_S and R_{ct2} from Pt and Pt/WO_3 CEs were obtained by fitting the experimental spectra with the equivalent circuit using Zview software, and are listed with the standard deviations in Table 1. It is obvious that R_S is smaller in Pt/WO_3 CE (4.53 ± 0.17 $\Omega\cdot cm^2$) than that in Pt CE (5.22 ± 0.06 $\Omega\cdot cm^2$), indicating the good contact between Pt/WO_3 CE and FTO due to the direct growth of WO_3 on FTO and the excellent electron transport in WO_3 nanoplate array. R_{ct2}, which associates with the catalytic property of a CE, is also lower in Pt/WO_3 CE (0.77 ± 0.01 $\Omega\cdot cm^2$) than in Pt CE (0.90 ± 0.02 $\Omega\cdot cm^2$). Since the R_{ct2} varies inversely with the catalytic activity, a lower R_{ct2} in Pt/WO_3 CE indicates a higher catalytic activity of Pt/WO_3 CE for I_3^- reduction.

Tafel polarization measurement is also a powerful method to characterize the electrochemical properties. Fig. 4c shows the Tafel plots of the symmetric cells similar to the one used in EIS measurement, which describes the dependence of electrical current density (J) on electrode potential. The exchange current density (J_0), which is directly related to the catalytic activity of the electrode, can be calculated from the intersection of the linear anodic and cathodic curves.[27] The relationship between the J_0 and R_{ct2} follows the equation below:

$$J_0 = \frac{RT}{nFR_{ct2}}$$

Where the R, T, F and N are the gas constant, the temperature, the Faraday's constant, and the number of electrons involved in the reduction of I_3^-, respectively. In consistent with EIS results, J_0 is obviously higher in Pt/WO_3 (9.5 ± 0.5 mA/cm^2) than in Pt CE (6.7 ± 0.1 mA/cm^2), indicating that the catalytic activity of Pt/WO_3 is superior over that of Pt CE.

As WO_3 on its own exhibits poor catalytic activity for I_3^- reduction, in the absence of variations in catalytic sites, the increased catalytic activity with the use of Pt/WO_3 CE must results from the modification of Pt nanoparticles and the electrode by the introduction of WO_3 nanoplate array.

A schematic illustration for the reduction process of I_3^- in Pt/WO_3 CE is depicted in Fig. 5. Fig. 5a displays the schematic structure of Pt/WO_3 CE on FTO, in which Pt nanoparticles dispersed discretely inner WO_3 nanoplate array due to the low Pt-loading. When the electrons generated from the photoanode are transported from the out circuit to FTO film, they will be injected in Pt/WO_3 CE and transported via WO_3 nanoplate before they are captured by I_3^- with the assistance Pt catalyst. The direct growth of WO_3 on FTO improves the interface contact, which makes the electron transfer from FTO to WO_3 much efficient. Moreover, the inherent good electron transport property of WO_3 and the direct electron transport path through WO_3 nanoplate enable the fast electron transport through WO_3 nanoplate array. In contrast, in the film composed of WO_3 nanoparticles, the physical contact at FTO/WO_3 interface and the boundaries between WO_3 nanoparticles retard electron transport and increase the recombination, and thereby, the DSC using Pt/WO_3 nanoparticles yields a low current density even in condition of a much thinner WO_3 nanoparticle film (<400 nm) than WO_3 nanoplate film (~600 nm). The efficient electron transfer in Pt/WO_3 nanoplate array is expected to be responsible for the low R_S in EIS measurement. Meanwhile, I_3^- diffuses into the porous WO_3 nanoplate array from the electrolyte. As the I_3^- reaches the surface of Pt nanoparticles, it captures two electrons and is reduced to $3I^-$ (as shown in Fig. 5b). The increased surface area by fine Pt nanoparticles and the facilitated diffusion of I^-/I_3^- redox sites in porous WO_3 nanoplate array increase the effective catalytic surface area, and thus reduces

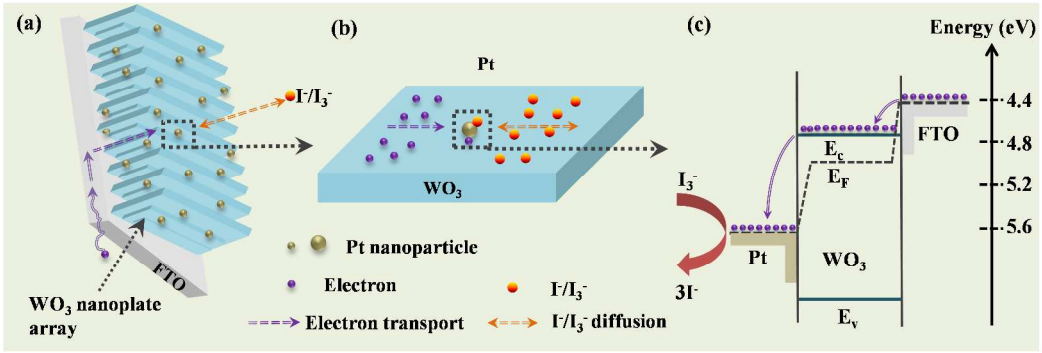

Fig. 5. Schematic illustration for the reduction process of I_3^-, (a) structure of Pt/WO_3 CE on FTO, (b) the electron transport and triiodide diffusion processes inside WO_3, and (c) energy level diagram of Pt/WO_3 CE on FTO.

R_{ct2}. Furthermore, from the energy level of Pt/WO_3 CE shown in Fig. 5c, it can be seen that electron injection is energetically favorable both from FTO to WO_3 and from WO_3 to Pt. It is worth noting that the electronic property of the supporter plays critical role in condition of low Pt-loading. In the case of nanomaterial with a higher Fermi level than the work function of FTO, it is not able to form the Ohmic contact at FTO/nanomaterial interface, which will hinder the electron injection from FTO to Pt. In fact, it is reported that in Pt/TiO_2/ITO electrode, the activity of the CEs decrease with increasing TiO_2 thickness to thicker than 25 nm,[14] which can be ascribed to the energy level mismatch between TiO_2 (n type with a conduction band at ~ 4.2 eV[19]) and ITO (with a work function of ~ 4.7 eV).

Hence, the excellent performance of DSC using Pt/WO_3 CE is attributed to the efficient electron injection and transport in CE/FTO, excellent energy level matching of Pt, WO_3 and FTO, nanostructure array morphology of WO_3 as well as better contact between WO_3 and FTO electrode. It can be speculated that other nanostructures, possessing these properties, can also be employed as ideal Pt supporters.

Furthermore, the obtained novel WO_3 nanostructure arrays and their composites with Pt are also ready to be used in other fields, such as electrochromic, hydrogen sensing, hydrogen evolution and other photoelectrochemical applications.

Conclusions

In summary, WO_3 nanoplate array is fabricated and used as Pt supporter for counter electrode in DSCs. It is demonstrated that Pt/WO_3 counter electrode possesses high electrochemical catalytic activity in catalyzing the reduction of triiodide to iodide, resulting in the high short circuit current density and power conversion efficiency of the related DSCs. The suitable energy level and the n-type property of WO_3 are crucial, which favor the efficient electron transfer from FTO to Pt. In addition, the large surface area of WO_3 nanoplate array also allows a lower consumption of expensive Pt material. Therefore, using Pt/WO_3 nanoplate array may foster the development of highly efficient DSCs. The results have also tremendous implications for future development of the highly catalytic and low-cost Pt based CEs.

Acknowledgements

This work was supported partially by the National Natural Science Foundation of China (Grant nos. 51372082, 51172069, 50972032, 61204064, 51202067 and 91333122), Ph.D. Programs Foundation of Ministry of Education of China (Grant nos. 20110036110006, 20120036120006, 20130036110012), Par-Eu Scholars Program, and the Fundamental Research Funds for the Central Universities.

Notes and references

[a] State Key Laboratory of Alternate Electrical Power System with Renewable Energy Sources, School of Renewable Energy, North China Electric Power University, Beijing 102206, China.
*Corresponding author: E-mail: mcli@ncepu.edu.cn; Fax: +86 10 6177 2951; Tel: +86 10 6177 2951..
[b] Chongqing Materials Research Institute, Chongqing 400707, China.
† Electronic supplementary information (ESI) available

1 M. Grätzel, *Acc. Chem. Res.*, 2009, 42, 1788−1798.
2 B. E. Hardin, H. J. Snaith and M. D. McGehee, *Nat. Photonics*, 2012, **6**, 162−169.
3 M. Liang and J. Chen, *Chem. Soc. Rev.*, 2013, **42**, 3453-3488.
4 M. Wu, X. Lin, T. Wang, J. Qiu and T. Ma, *Energy Environ. Sci.*, 2011, **4**, 2308.
5 J Zhang, S Najmaei, H Lin and J Lou, *Nanoscale*, 2014, **6**, 5279-5283.
6 L. X. Yi, Y. Y. Liu, N. L. Yang, Z. Y. Tang, H. J. Zhao, G. H. Ma, Z. G. Su and D. Wang, *Energy Environ. Sci.*, 2013, **6**, 835−840.
7 D. Song, M. Li, Y. Li, X. Zhao, B. Jiang and Y. Jiang, *ACS Appl. Mater. Interfaces*, 2014, **6**, 7126−7132.
8 H. Jeong, Y. Pak, Y. Hwang, H. Song, K. H. Lee, H. C. Ko and G. Y. Jung, *Small*, 2012, **8**, 3757–3761.
9 C. C. Yang, H. Q. Zhang and Y. R. Zheng, *Curr. Appl. Phys.*, 2011, **11**, S147eS153.
10 G. T. Yue, J. H. Wu, Y. M. Xiao, M. L. Huang, J. M. Lin, L. Q. Fan and Z. Lan, *Electrochim. Acta*, 2013, **92**, 64−70.
11 S. Mukherjee, B. Ramalingam, L. Griggs, S. Hamm, G. A. Baker, P. Fraundorf, S. Sengupta and S. Gangopadhyay, *Nanotechnology*, 2012, **23**, 485405.
12 B. Ramalingam, S. Mukherjee, C. J. Mathai, K. Gangopadhyay and S. Gangopadhyay, *Nanotechnology*, 2013, **24**, 205602.

13 P. T. Shih, R. X. Dong, S. Y. Shen, R. Vittal, J. J. Lin and K. C. Ho, *J. Mater. Chem. A*, 2014, **2**, 8742.
14 K. C. Huang, Y. C. Wang, R. X. Dong, W. C. Tsai, K. W. Tsai, C. C. Wang, Y. H. Chen, R. Vittal, J. J. Lin and K. C. Ho, *J. Mater. Chem.*, 2010, **20**, 4067–4073.
15 N. Q. Fu, Y. Y. Fang, Y. D. Duan, X. W. Zhou, X. R. Xiao and Y. Lin, *ACS NANO*, 2012, **6**, 9596−9605.
16 C. P. Cho, H. Y. Wu and C. C. Lin, *Electrochim. Acta*, 2013, **107**, 488–493.
17 C. A. Bignozzi, S. Caramori, V. Cristino, R. Argazzi, L. Meda and A. Tacca, *Chem. Soc. Rev.*, 2013, **42**, 2228−2246.
18 H. Qi, J. Wolfe, D. Wang, H. J. Fan, D. Fichou and Z. Chen, *Nanoscale*, 2014, **6**, 13457-13462.
19 M. Grätzel, *Nature*, 2001, **414**, 338−344
20 J. Y. Zheng, G. Song, C. W. Kim and Y. S. Kang, *Nanoscale*, 2013, **5**, 5279-5282.
21 F. Amano, D. Li and B. Ohtani, *Chem. Commun.*, 2010, **46**, 2769−2771.
22 J. Yang, W. Li, J. Li, D. Sun and Q. Chen, *J. Mater. Chem.*, 2012, **22**, 17744.
23 X. X. Li, G. Y. Zhang, F. Y. Cheng, B. Guo and J. Chen, *J. Electrochem. Soc.*, 2006, **153**, H133.
24 L. Han, N. Koide, Y. Chiba and T. Mitate, *Appl. Phys. Lett.*, 2004, **84**, 2433.
25 A. Haucha and A. Georg, *Electrochim. Acta*, 2001, **46**, 3457–3466.
26 Q. Wang, J. E. Moser and M. Grätzel, *J. Phys. Chem. B*, 2005, **109**, 14945−14953.
27 A. J. Bard and L. R. Faulkner, Electrochemical Methods: Fundamentals and Applications, 2nd ed.; John Wiley & Sons: New York, 2000, 103−104.